FEA-Based Failure Analysis of Post-Buckled Composite Multi-Hat Stiffened Panel Under Static Compression

ABSTRACT

The aerospace industry uses composite multi-hat stiffened panels for skins because of their high strength-to-weight and stiffness-to-weight ratios. However, laminated composites with initial flaws are susceptible to delamination under buckling loads. The goal is to ensure damage initiation occurs past the buckled state, only stable damage progression at loads below the ultimate compressive load, and debonding failure past the ultimate compressive load. This approach reduces weight and addresses a potential design review for future aircraft repairs. The need exists to better understand damage initiation and growth mechanisms in composite structures while assisting in the design, analysis, and sustainment methods. Teflon inserts simulate damage defects during manufacturing, while barely visible impact helps capture human error during manufacturing. This work shows the interaction between the skin-stringer and ply-ply separations at the post-buckled state for both defect events using Abaqus Virtual Crack Closure Technique (VCCT). The initial configuration for the Teflon case was to leave the Teflon region unbonded, and the initial impact damage region approximation came from the experimental data and was considered the initial configuration. When compared against the experimental data produced through the NASA Advanced Composites Project (ACP), the present model captured damage transition from skin-hat to ply1-ply2. The model validations were within ~5% of the experimental data.

Vijay K. Goyal, Lockheed Martin Aeronautics, Marietta, U.S.A
Austin Pennington, Lockheed Martin Aeronautics, Fort Worth, TX, U.S.A

INTRODUCTION

Composite materials are an increasingly important advancement in aerospace because they play an essential role in weight reduction. Therefore, advanced composites consisting of high-strength stiff fibers embedded in a common matrix material are also widely used in the aerospace industry. Their advantages include high specific strength, lightweight, resistance to fatigue and corrosion, and their ability to be tailored for various designs. The design of laminated composite panels should provide good buckling capacity. Shear force, compressive load, and the combination can be applied to the panel to check its stability. Generally, local buckling, global buckling, and collapse occur under stiffened panels' shear and compression loading scenarios.

Using hat-stiffened panels is one design option that can meet the high stiffness and minimal weight requirements. Composite hat-stiffened panels are a dominant part of airframes because of their excellent anti-buckling capabilities, significantly improving structural stability. However, when designing multi-hat stiffened composite panels, debonding between the skin and the hat, or even between the skin plies, is a failure concern. Moreover, aircraft may be designed in the skin postbuckled region, resulting in a lightweight aircraft. Hence, understanding the damage initiation of a full-scale panel and its local-global failure is a challenging event (Degenhardt et al. [1]; Hao et al. [2]; Gliszczynski et al. [3]; Pietropaoli and Riccio [4]; Gong et al. [5]; Gong et al. [6]).

This failure prediction is challenging because of the interaction of the post-buckling deformation with different failure modes, such as interlaminar damage, delamination, and skin-stiffener delamination (Bisagni et al. [7]; Anyfantis and Tsouvalis [8]). Delamination, particularly the separation of the skin-stiffener and ply-ply, is the most common and critical damage in stiffened panels in the post-buckled regimen. One used to study PDA is the Virtual Crack Closure Technique (VCCT) (De Carvalho et al. [9]; Mabson et al. [10]; Di Memmo and Bisagni [11]; Raimondo et al. [12]; Camanho et al. [13]). The one drawback is the identification of the crack initiation, which can be identified using the Cohesive Zone Model (CZM) and then switching to VCCT (Goyal et al. [14-15]).

Goyal et al. [14-15] used VCCT to predict damage initiation and propagation of a single-hat stiffened panel under BVI and Teflon insert. Their VCCT methodology in Abaqus showed results were within 5% when compared with experimental data conducted through the NASA Advanced Composites Project (ACP) (Leone et al. [16]; Leone et al. [17]). This work extends that work to multi-hat stiffened panels subjected to static compression loading for the following cases: (i) Panel with a known flaw (Teflon insert), and (ii) panel with initial impact damage. In this work, loads are nondimensionalized by dividing the values by an average peak value from the Teflon test configuration, called $P*$. Likewise, displacements are nondimensionalized by a displacement corresponding to a value slightly past the point of failure for the Teflon test configuration, called $U*$.

TESTING CONFIGURATION

This work focused on co-cured multi-hat stiffened panels designed to carry the compressive load into a post-buckled state and fabricated as well as tested under the NASA ACP. The specimens, shown in Figure 1, consisted of four hat-section stiffeners and a representative skin panel (Action et al. [18]).

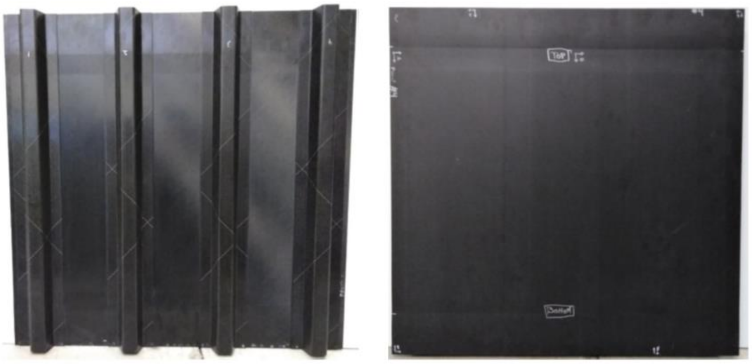

Figure 1. Multi-Hat Stiffened Panels

The hat stiffeners were made of four inner-wrap plain weave (PW) fabric carbon fiber-reinforced epoxy (CFRP) plies with lay-up $[45/-45/0/45]_T$, an over-wrap of twelve PW fabric CFRP plies with lay-up $[45/-45/0/45/45/0/-45/45/45/-45/0/45]_T$, and a filled epoxy noodle section. The skin panels were laid-up as $[-45/45/0/90/-45/45/]_S$ from twelve unidirectional tape CFRP plies. All ply orientations are referenced to a 0-degree direction parallel to the longitudinal stiffener axis. Integrated pad-ups at the ends of the panels doubled the ply count symmetrically and followed a 20:1 drop-off rate into the acreage. These pad-ups promoted buckling and failure away from the specimen boundary conditions. Due to a slight manufacturing defect, there was a joggle in the skin between the ramp and acreage. Additionally, the curing process resulted in slight global warpage of the panel. The assembly was prepped for testing by potting the ends into Aluminum plates using an adhesive.

Seven-panel assemblies were fabricated for static testing in the NASA ACP. Three specimens were imparted initial impact damage prior to static compression. The remaining four were fabricated with two embedded Teflon strips between the hat stiffener flanges and skin panel meant to initiate delamination in the post-buckled state. The impact-damage specimens are shown in Figure 2(a), and the Teflon-insert specimens are shown in Figure 2(b).

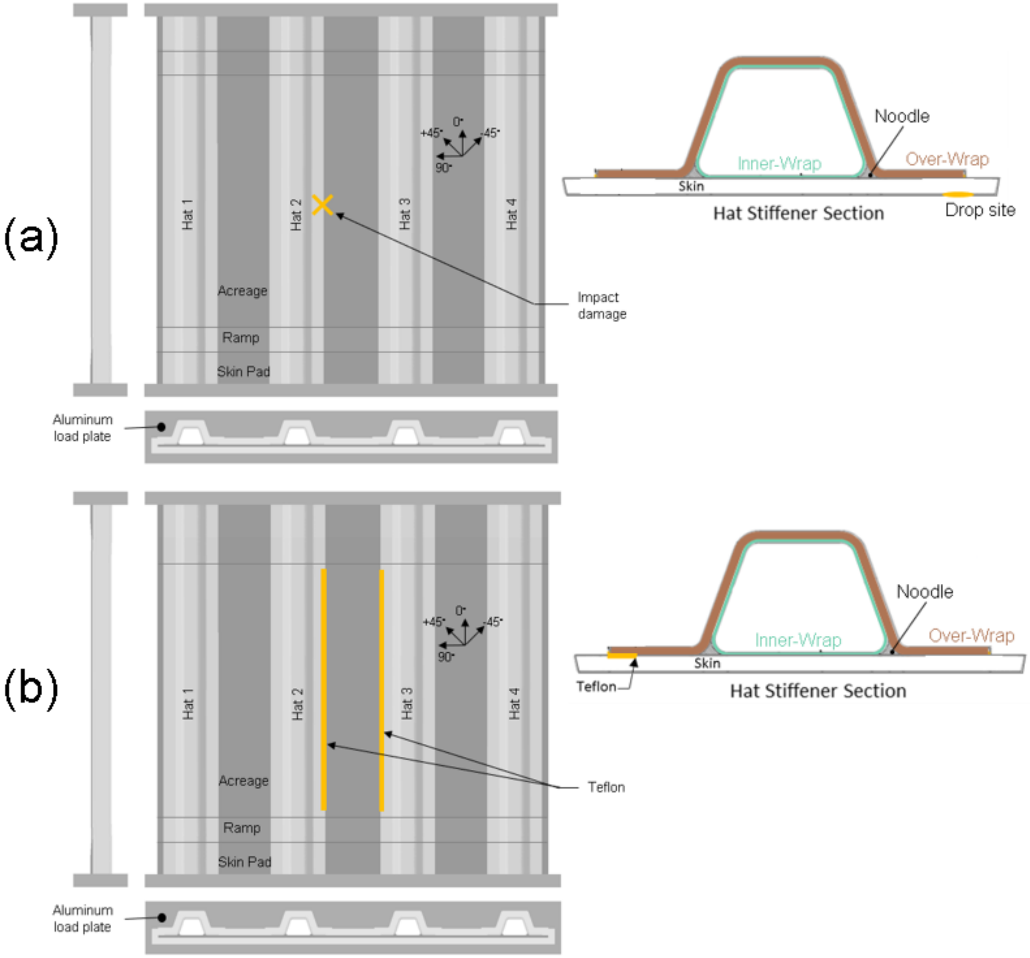

Figure 2. (a) Impact-Damaged Specimen Geometry, (b) Teflon-Insert Specimen Geometry

Initial damage was introduced via a low-velocity drop-weight impactor prior to compressive loading for the three impact-damaged panels. The impactor device was stainless steel with a 1-inch diameter hemispherical tip weighing 3.82 lb. The specimen was supported on the hat-stiffener side with a 3D-printed holder during the impact event, shown in Figure 3(a). The weight was dropped on either the second or third stiffener, or both, depending on the specimen, at the panel's lengthwise midpoint, on the skin side of the specimen, and approximately 0.20 inches away from the hat flange's edge towards the longitudinal center of the stiffener, as shown in Figure 3(a). The reason for impacting one specimen twice was because the damage after the first impact was minimal. The energy imparted by the impact ranged from 5 to 8 ft-lb. The resulting damage was primarily observed in the first (from the top) skin ply interface, with additional damage occurring in the skin-hat interface, connected to the skin delamination via a series of matrix cracks in the first skin ply. Ultrasonic (UT) inspection results are depicted in Figure 3(b), while Table 1 contains the breakdown of impact characterization and damage for each specimen.

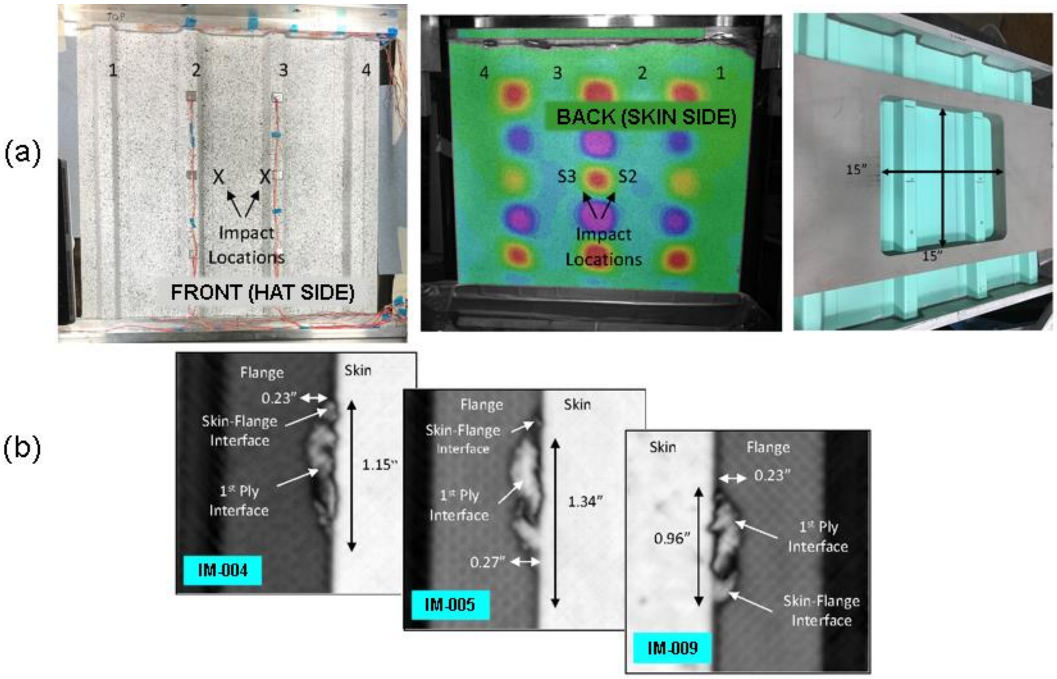

Figure 3. (a) L to R: Impact Locations Shown from Front, Impact Locations Shown from Back, Impact Event Fixture with Specimen, (b) UT Inspection Scans of Initial Impact Damage on Static Panels

Table 1. Initial Impact Characterization

Specimen ID	Impacted Stiffener	Drop Height [in]	Nominal Energy [Ft-lbs]	Damage Width [in]	Damage Length [in]
ACC18-4SP-IM-004	S2	16.5	5.2	0.08	0.63
	S3	24.0	8.0	0.29	1.19
ACC18-4SP-IM-005	S3	25.0	8.0	0.30	1.35
ACC18-4SP-IM-009	S2	16.5	5.25	0.23	0.94

The specimens were end-loaded in compression via displacement control using a 220-kip MTS servo-hydraulic frame. Steel loading platens on each end of the vertically-aligned specimen resisted deformation and rotation and allowed fine-tuning to achieve an even side-to-side loading distribution. A loading rate of 0.025-in/min was followed to P/P*=0.262, at which point head leveling was performed, then continued to P/P*=0.613. Subsequently, loading was continued at a rate of 0.01-in/min. Some specimens were loaded continuously to failure, using only in-situ monitoring, while the rest were loaded incrementally, with UT inspection at pauses. Pauses were determined using passive thermography, acoustic emission (AE) results, and pre-determined loads.

Instrumentation used in the testing included twenty-eight back-to-back axial strain gauges placed on both sides of the panel, two-sided digital image correlation (DIC), six AE sensors, and passive thermography. These instruments are depicted in Figure 4.

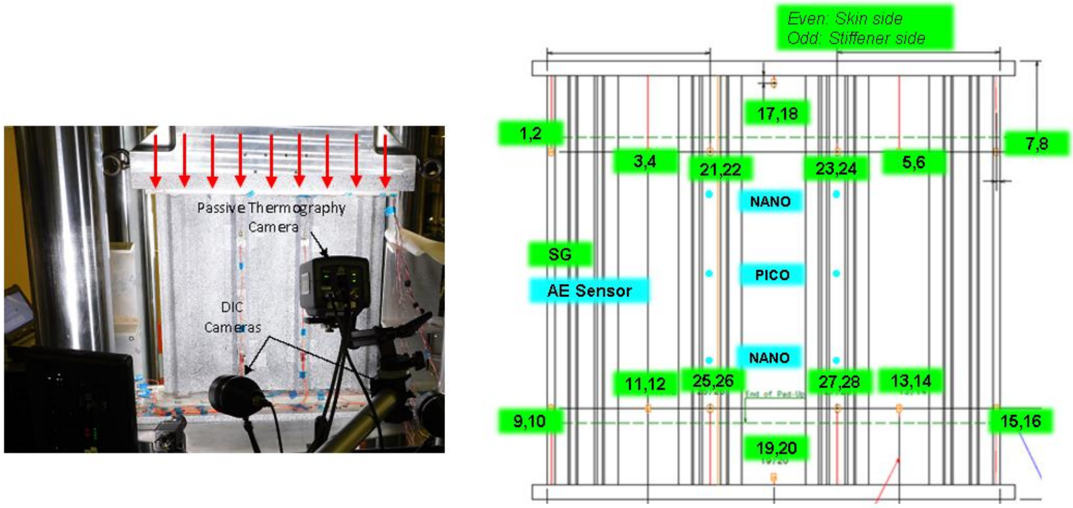

Figure 4. Multi-Hat Stiffened Panel Instrumentation

Table 2 lists tested specimens and the scaled peak loads for each statically-loaded multi-hat stiffened panel. The specimens buckled first in the center panel bay at an average critical buckling load of P/P*=0.391. The buckling mode shape consisted of five half-waves of a down-up-down-up-down variety, where "down" corresponds to a deflection of the skin away from the stiffeners. Subsequently, the outer skin bays also buckled at an average load of P/P*=0.670. These buckling shapes were similar to those first experienced in the center bay. In the Teflon specimens, delamination between the skin and hat stiffener began at the edge of the Teflon inserts in the middle of the panel due to the buckling shape of the skin. This "down" wave effectively peeled the skin panel away from the hat stiffener flanges. As determined from passive thermography and limited by its resolution, the damage initiation load was P/P*=0.937 in specimen ACC18-4SC-INS-003. From the incremental UT scans of ACC18-SP-INS-011, the initial P/P* appears to occur between 0.954 and 0.981. The skin-hat delamination was observed to migrate into the first ply interface of the skin panel, with a series of matrix cracks in the first skin ply connecting the two damage zones. After a short period of stable delamination growth, the panels failed catastrophically.

Table 2. Mutli-Stringer Panel Test Results

Specimen ID	Initial Defect Type	Peak Load (P/P*)
ACC18-4SP-IM-004	Impact	1.089
ACC18-4SP-IM-005	Impact	1.080
ACC18-4SP-IM-009	Impact	1.033
ACC18-4SP-INS-002	Teflon	1.012
ACC18-4SP-INS-003	Teflon	0.982
ACC18-4SP-INS-010	Teflon	0.981
ACC18-4SP-INS-011	Teflon	1.024

Similarly, the impact-damaged specimens experienced additional delamination growth in the skin-hat and skin-first interface planes prior to catastrophic failure. For specimen ACC18-4SP-IM-009, on which the present modeling is based, the passive thermography system captured damage growth at P/P*=0.876. Figure 5(a) shows the buckling events prior to panel failure characteristic of all statically-loaded panels. Figure 5(b) shows the incremental failure events of Teflon specimen ACC18-SP-INS-011.

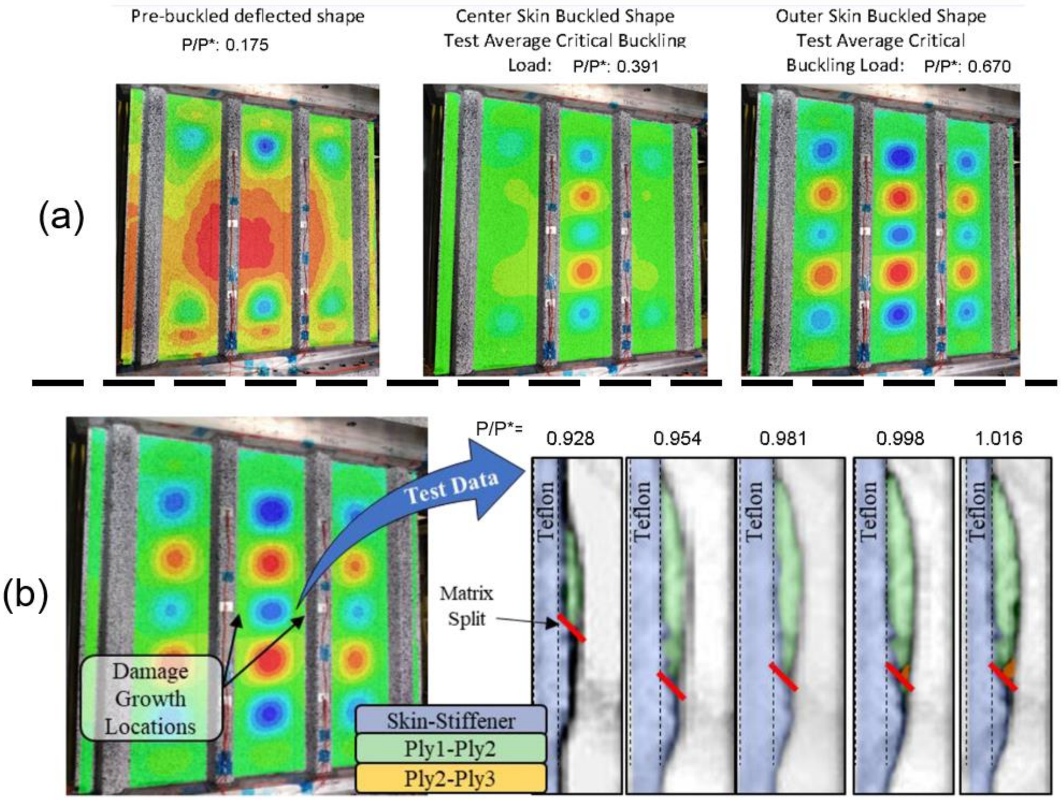

Figure 5. (a) Panel Buckling – DIC indicating out-of-plane displacements, (b) Failure Events – Specimen ACC18-4SP-INS-011. (Test data from Action et al. [18])

INTERLAMINAR FAILURE PREDICTION USING VCCT

The current effort sought to align PDA predictions using VCCT in Abaqus to the test results presented previously by Action et al. [18]. The finite element model (FEM) used Abaqus for preprocessing, processing, and post-processing. The specimen was modeled with continuum shell elements (SC8R) for all composite plies and solid elements (C3D8R) for all other components. The end regions, skin acreage, and stringers 1 and 4 were meshed with 0.25-inch in-plane seeding, and one element through the thickness as they intended only to provide a representative stiffness to the regions of damage analysis. The element edge lengths in the refined regions (stringers 2 and 3) were 0.10-inches, while the element widths (global z-direction) were 0.04-inches. As discussed later, the mesh densities for the center skin bay and damage regions were higher and varied through the analysis to create refinement levels. The VCCT assignments only applied to the model's damaged regions to minimize the required model size. The size of these regions was chosen to provide enough area for the delamination to grow to the critical point where the peak load of the panel was reached, and the catastrophic failure commenced. The damage regions of the model were tied at their edges to the refined regions, which were tied to the acreage regions of the panel. A lateral and axial stress-free warpage transverse to the stiffeners in a parabolic shape was applied to the model by modifying the nodal coordinates before analysis. This helped account for the as-cured geometry of the assembled panels. The steel loading platen on the top end of the specimen was modeled with solid elements and assigned contact with friction to the top surface of the specimen and load plate. A general arrangement of the FEM is provided in Figure 6.

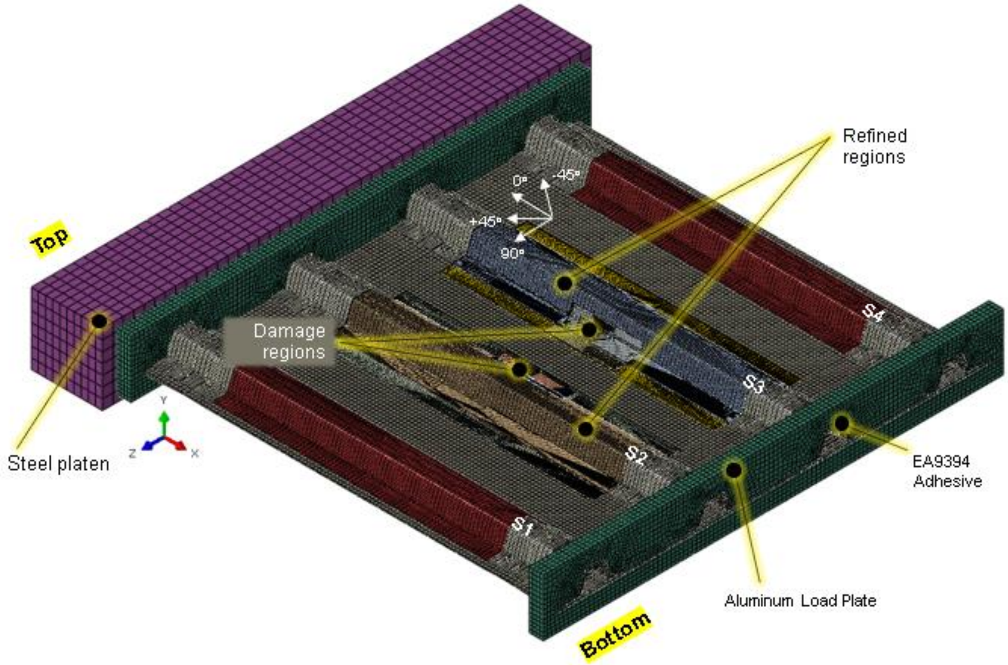

Figure 6. FEM General Arrangement

The model boundary conditions were defined in terms of displacement constraints and prescriptions. The axial (x) direction was constrained by assigning zero displacements to the entire bottom surface. The top surface of the steel platen was prescribed an axial compressive displacement. By the nature of these conditions, both top and bottom surfaces were constrained against rotation. The top surface of the steel platen and lower surface of the specimen were also assigned zero displacement conditions in the y- and z-directions.

Figure 7 shows the skin pad-ups on both the top and bottom ends of the specimen were represented along with the manufacturing defect/joggle in the ramp-down regions. The aluminum load plates and substantial layer of potting material, EA9394 adhesive, were also modeled and tied rigidly to the specimen ends.

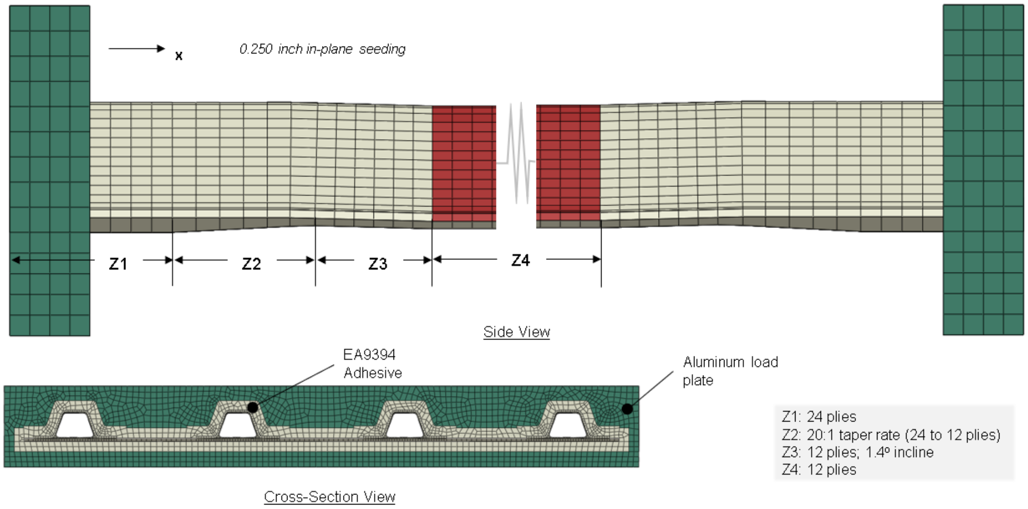

Figure 7. FEM End Region Details

The damage regions of the model, as discussed previously, were tied to the surrounding mesh, allowing for focused refinement. The in-plane element edge length in the center skin bay was also shortened from its baseline 0.25-inch value for certain refinement levels. In these damage regions, the first skin ply was modeled with a discrete layer of elements, as was the second skin ply. Figure 8 shows the damaged regions and an exploded view of the one within stringer 2 (S2).

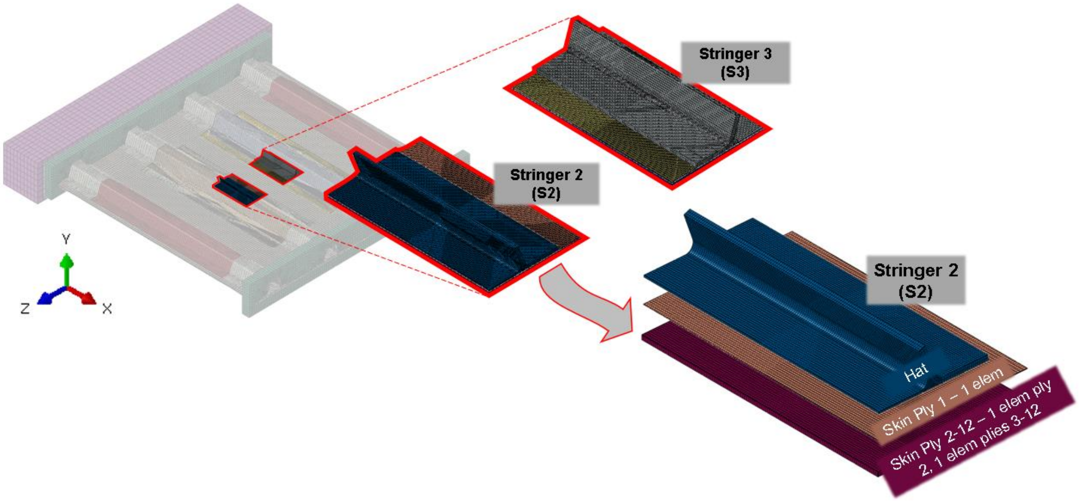

Figure 8. Multi-Hat Stiffened Panel FEM Damage Region Detail

A summary of the mesh sizes for model refinement levels corresponding to the Teflon specimen is given in Table 3 and Table 4 for the Impact versions. Here, all dimensions are given in inches, and the term "Hat TT" refers to the number of elements through the thickness of the hat over-wrap layer. "Acreage" refers to the in-plane element edge-length assigned to the skin elements in the center bay adjacent to the damaged regions.

Table 3. Mesh Sizes for Teflon Models TR0-TR3

Teflon	S2 & S3			Acreage
Name	Width	Length	# Hat TT	
TR0	0.060	0.060	2	0.250
TR1	0.040	0.040	2	0.250
TR2	0.020	0.020	2	0.125
TR3	0.010	0.010	4	0.063

Table 4. Mesh Sizes for Impact Models IR1-IR3

Impact	S2 (Impact damage site)			S3			Acreage
Name	Width	Length	# Hat TT	Width	Length	# Hat TT	
IR1	0.030	0.030	2	0.040	0.040	2	0.125
IR2	0.020	0.020	2	0.040	0.040	2	0.125
IR3	0.015	0.015	4	0.040	0.040	2	0.125

For the Impact-damaged specimen analysis, the initial damage in specimen ACC18-4SP-IM-009 was modeled. This specimen was impacted only on stringer 2. Therefore, VCCT interactions were only implemented in the refined regions of this stringer. Two distinct VCCT interactions were established, as shown in Figure 9; the first between the hat stiffener and skin ply 1 elements, and the second between the skin ply 1 elements and skin ply 2 elements.

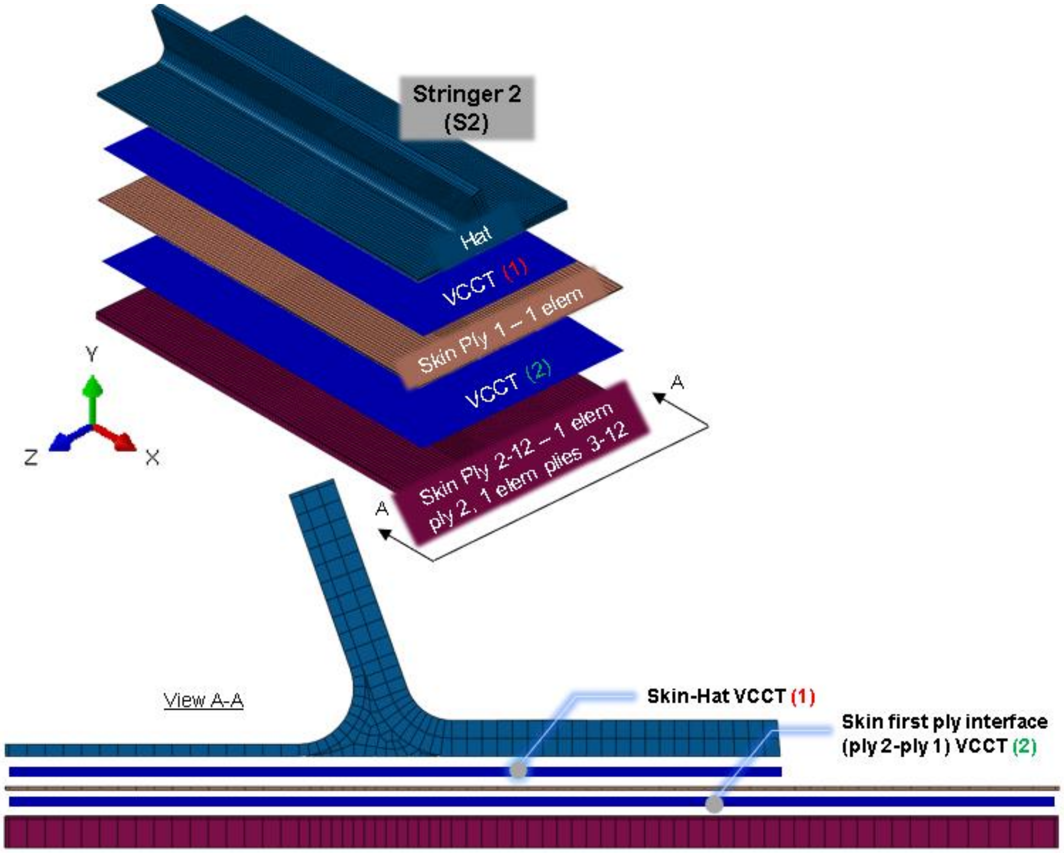

Figure 9. Impact-Damage Refined Region VCCT

The UT scan in Figure 10(a) revealed that the initial damage due to the impact event for specimen ACC18-4SP-IM-009 was 0.96-inches long and 0.23-inches wide, where length indicates the dimension parallel to the loading direction. The VCCT routine in Abaqus requires the user to define nodes in the initially bonded zone. This designates an initially unbonded zone from which the delamination progresses. The scan was overlaid onto a sketch plane in Abaqus/CAE to define the boundaries of these zones. The delamination between the first two skin plies is depicted in green in Figure 10(b). This delamination migrated via matrix cracks into the skin-hat interface. Since VCCT only simulates intralaminar debonding and not interlaminar damage, an alternate approach was implemented to capture the effects of degraded matrix stiffness local to the migration zone. The matrix-dominated moduli (E_{22}, E_{33}, G_{13}, and G_{23}) of the elements constituting the first skin ply in this small diagonal (aligned with the +45 ply orientation of skin ply 1) strip were lowered by 75% to mimic the reduced stiffness caused by the damage. The skin-hat delamination is shown in red in Figure 10(b).

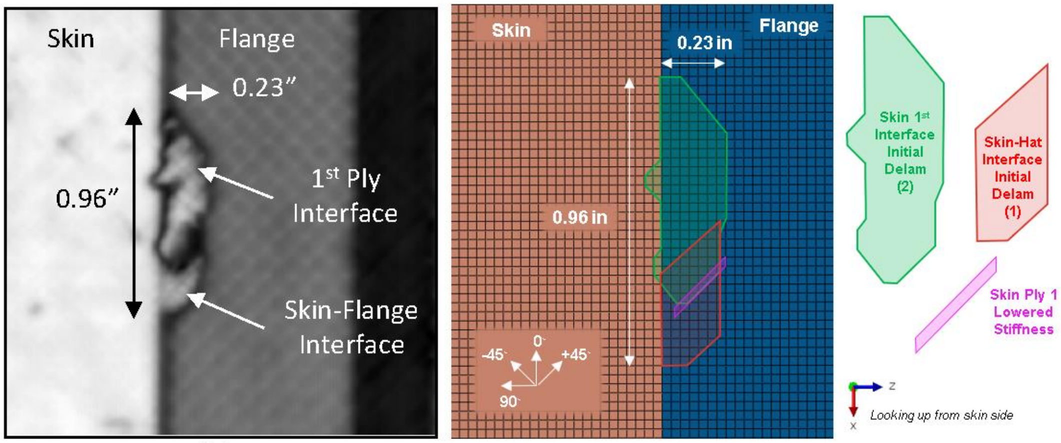

(a)
Ultrasonic images viewed from skin side
Specimen ACC18-4SP-IM-009
After impact, before compression

(b)
FE Model (Refinement level 1: 0.03” in-plane edge length)
Initial Delam indicates excluded nodes from “Initially bonded” node sets
Lowered Stiffness indicates elements with matrix cracking

Figure 10. Impact-Damaged Specimen Initial Damage Model.

The static fracture toughness properties for the tape-tape and tape-fabric interfaces used here are based upon the previous work on single-hat stiffened panels by Goyal et al. [14-15]. A summary of the properties is given in Table 5.

Table 5. Fracture Toughness Properties used in Models

Interface	$G_{IC}/G_{C}*$	$G_{IIC}/G_{C}*=G_{IIIC}/G_{C}*$
Tape-Fabric	1.25	5.85
Tape-Tape	1.00	3.08

$G_{C}*= G_{IC}$ for tape-tape

For the Teflon-insert specimen model, two distinct VCCT interactions were established within both the refined region in stringer 2 and stringer 3, as shown in Figure 11(a). These interactions were between the hat stiffener and skin ply 1 elements and between the skin ply 1 elements and skin ply 2 elements. As for the initially bonded zones depicted in Figure 11(b), in the skin-hat plane, excluded nodes fell within the zone of the surface corresponding to the Teflon insert at the edges of the hat flanges in the center panel bay. In the skin first interface plane, excluded nodes were a defined distance away from the Teflon edge in a small strip. In lieu of a simulated delamination migration from the skin-hat interface to the skin first-ply interface, which is not a feature of VCCT, a delamination initiation zone for the skin first interface was chosen based on observation of test behavior. Once the delamination in the skin-hat interface grew inward to the skin first interface initiation zone, delamination growth in the skin became the dominant factor in panel failure.

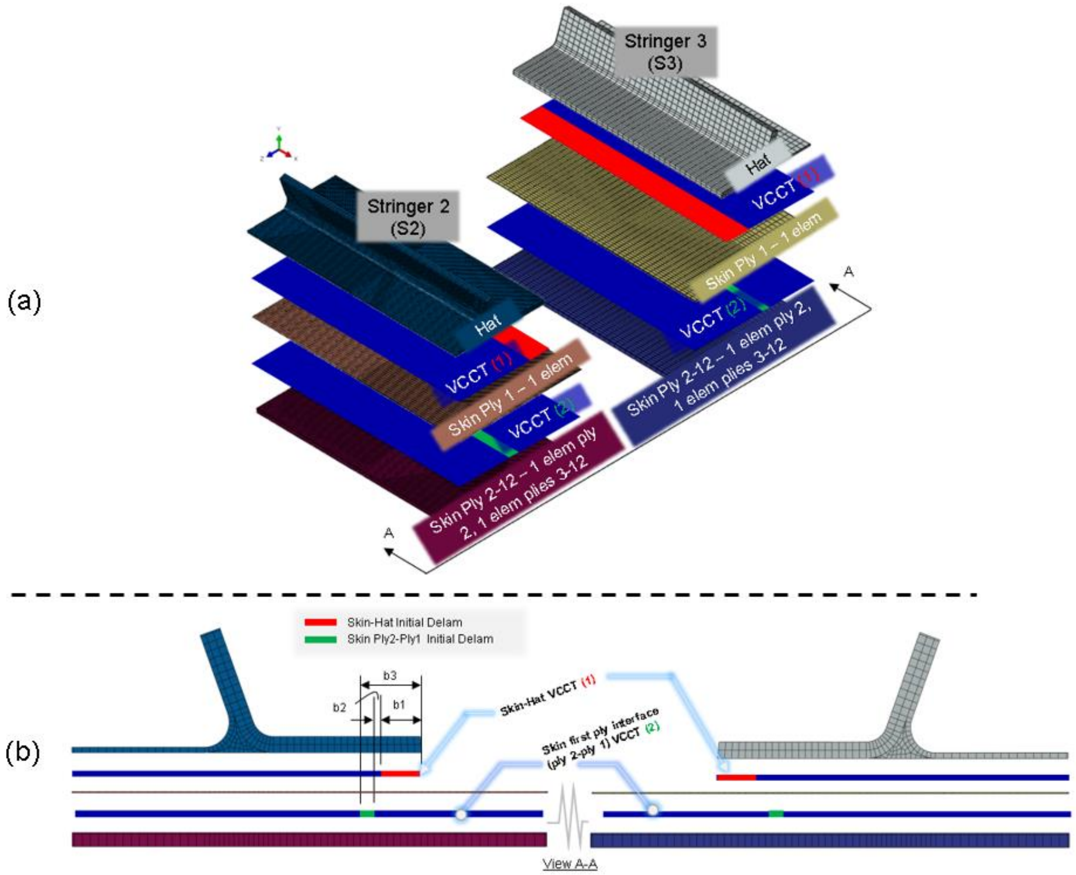

Figure 11. Teflon Specimen, (a) VCCT Interaction Assignments, (b) Initially Bonded/Unbonded Zones

The Benzeggagh-Keane (B-K) mixed-mode criterion was used for all VCCT analyses. The default unstable growth tolerance (UGT) of infinity and a VCCT tolerance of 0.10 was used as a baseline. The "Step" debonding method was implemented at the outset of the project, but the "Ramp" method was subsequently investigated. Contact controls were implemented with a value of 1.E-06 for the damping factor.

All models were run on an HPC with 24 cores unless otherwise noted. The version of Abaqus used for the solution was Abaqus 2021.HF7. Both Abaqus/Standard and Abaqus/Explicit were used to compare results. The Abaqus/Standard runs used geometrically nonlinear analysis and unsymmetric matrix storage and solution. For Abaqus/Explicit runs, an end displacement of U/U*=1.3043 over 8 seconds according to a "smooth step" amplitude, dampening the velocity at the beginning and end of the analysis to encourage quasi-static behavior, was applied. Variable mass scaling with an element stable time increment of 5e-06 was also used.

RESULTS

The multi-hat stiffened panel FE model was evaluated first by comparing model strain outputs to strain gauge (SG) readings from a representative test conducted in the NASA ACP for calibration purposes. Given in Figure 12 is a comparison of strains at SG locations 3 and 4. First, average strains were calculated for these back-to-back gauges to mitigate more sensitive bending effects and compared the test and FEM results. As shown, the analysis average curve matched well with the test results. Next, a pre-buckled pseudo-stiffness (the ratio of change in total panel load to local strain change) was calculated for the region below the average critical buckling scaled load of 0.391. For SG pairs 3&4, the pre-buckled average stiffness in the FEM was within 1.5% of the test.

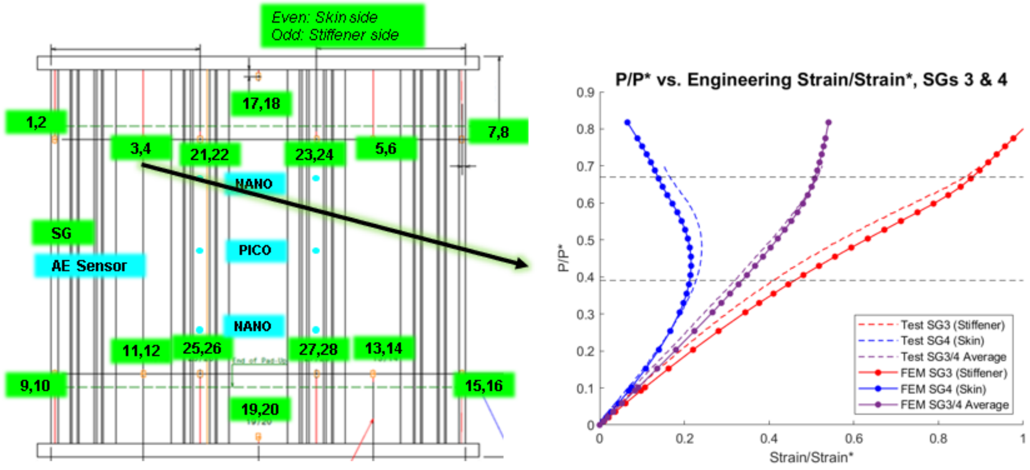

Figure 12. Strain Comparison between FEM and Test; Gauges 3 and 4

Table 6 compares test and analysis for each strain gauge pair's average pre-buckled behavior. The stiffness percentage error for all SG pairs falls within 6% except pairs 1&2, 7&8, 9&10, and 15&16. These locations are on the four corners of the panel, far away from the damage regions of interest in the middle of the panel, and are therefore not of great concern in relation to the damage analysis.

Table 6. Strain Gauge Stiffness Comparison

SGs	K_{test}	K_{FEM}	% Error	SGs	K_{test}	K_{FEM}	% Error
	[(lb/lb)/(με/με)]				[(lb/lb)/(με/με)]		
1&2	1.36	1.20	-12.1	13&14	1.27	1.19	-6.1
3&4	1.19	1.18	-1.4	15&16	1.43	1.19	-16.6
5&6	1.22	1.19	-2.7	17&18	2.51	2.59	+3.2
7&8	1.38	1.20	-13.0	19&20	2.49	2.62	+5.1
9&10	1.37	1.20	-12.5	21&22	1.15	1.10	-4.9
11&12	1.17	1.18	+1.4	23&24	1.16	1.09	-5.3

Additionally, the buckling behavior of the panel as simulated in the FE analysis was compared to the average buckling loads observed in the test. The critical buckling loads for the middle and outer panel bays were evaluated in the FEM results using three methods. The first, shown in Figure 13, was to plot the panel load against back-to-back strains for the point of interest and note where the two curves diverge to indicate local buckling. The second was to plot out-of-plane displacements against the panel load and observe where the curves became nonlinear. For the middle bay, the first method revealed a FEM critical scaled buckling load of 0.442, while the second gave 0.454. Compared to a test average critical buckling scaled load of 0.391, the FEM had an average critical buckling load for the middle bay of 15% over the test average. For the outer bay, the first method gave a FEM critical scaled load of 0.563, while the second gave 0.574. Compared to a test average critical buckling scaled load of 0.670, the FEM had an average scaled buckling load for the outer bay of 15% less than the test average.

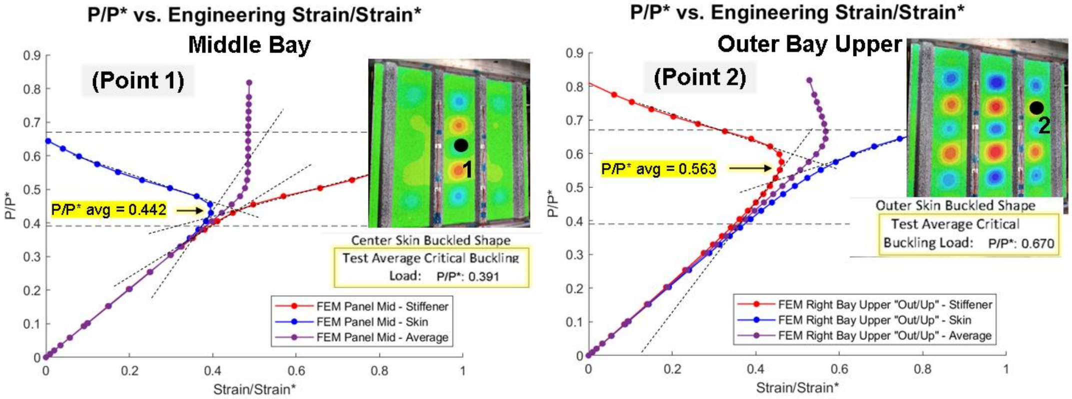
P/P* vs. Engineering Strain/Strain* Middle Bay

(Point 1)

P/P* avg = 0.442

Center Skin Buckled Shape

Test Average Critical Buckling Load: P/P*: 0.391

P/P* vs. Engineering Strain/Strain* Outer Bay Upper

(Point 2)

P/P* avg = 0.563

Outer Skin Buckled Shape

Test Average Critical Buckling Load: P/P*: 0.670

Figure 13. FEM vs. Test Critical Buckling Loads Comparisons

The third method to identify model buckling was to compare the out-of-plane fringe plots to the DIC images from the test, as shown in Figure 14. This yielded a middle bay scaled buckling load of approximately 0.479 and an outer bay scaled buckling load of 0.688, corresponding to +23% and +3% errors, respectively. Ultimately, since the determination of buckling is somewhat subjective in that it occurs over a load range and not a single point, the model efficacy was judged to be valid in this regard.

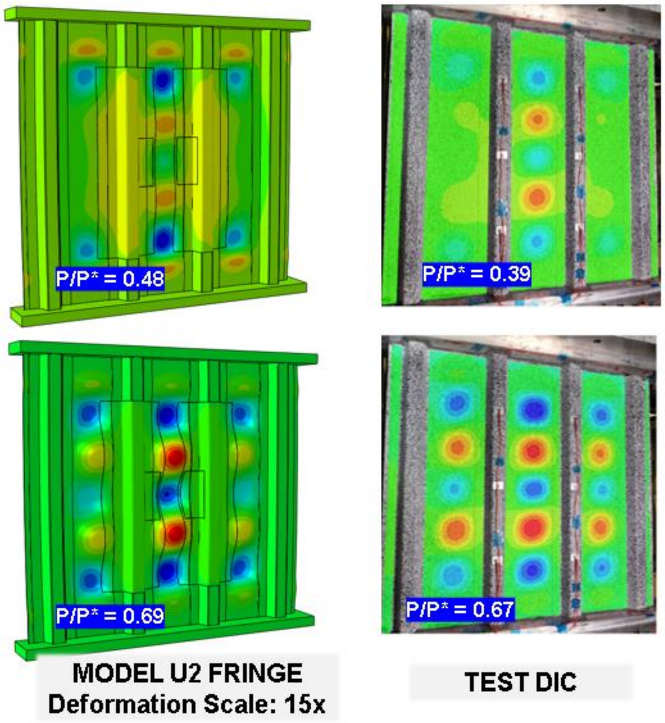

Figure 14. Model vs. Test Buckling Fringe plots

In general, the analyses in Abaqus/Standard using the Step debonding force produced peak loads 10-15% below those from the Ramp debonding force runs. The Step debonding method releases the residual force at debonding nodes instantaneously, while the Ramp method ramps the force down gradually, creating a more accurate simulation. The analyses in Abaqus/Explicit generally produced peak loads higher than the Step runs and similar to, or below, the Ramp runs. Abaqus/Explicit presents additional challenges in ensuring a quasi-static solution in the time domain. Due to these comparisons, the Ramp debonding method used in conjunction with Abaqus/Standard was chosen as the preferred approach for simulation.

The Impact-damaged panel, ACC18-4SP-IM-009, on which the modeled initial damage was based, failed at a peak scaled load of 1.033. As demonstrated in Figure 15, the Abaqus/Standard runs initiated delamination in the Skin-Hat interface at a scaled load level of 0.671, before experiencing stable growth, including additional growth in the Skin Ply 2-Ply 1 interface initiating at 0.733. This initiation load was lower than the scaled observed onset load from the test, which was 0.876. However, since the initiation occurred in the skin-hat interface beneath the skin first interface delamination, it would evade the passive thermography system set-up. Similarly, the initiation in the skin first interface is so minuscule that it is difficult to compare to the test observations directly. The Ramp run saw a scaled peak load of 1.045.

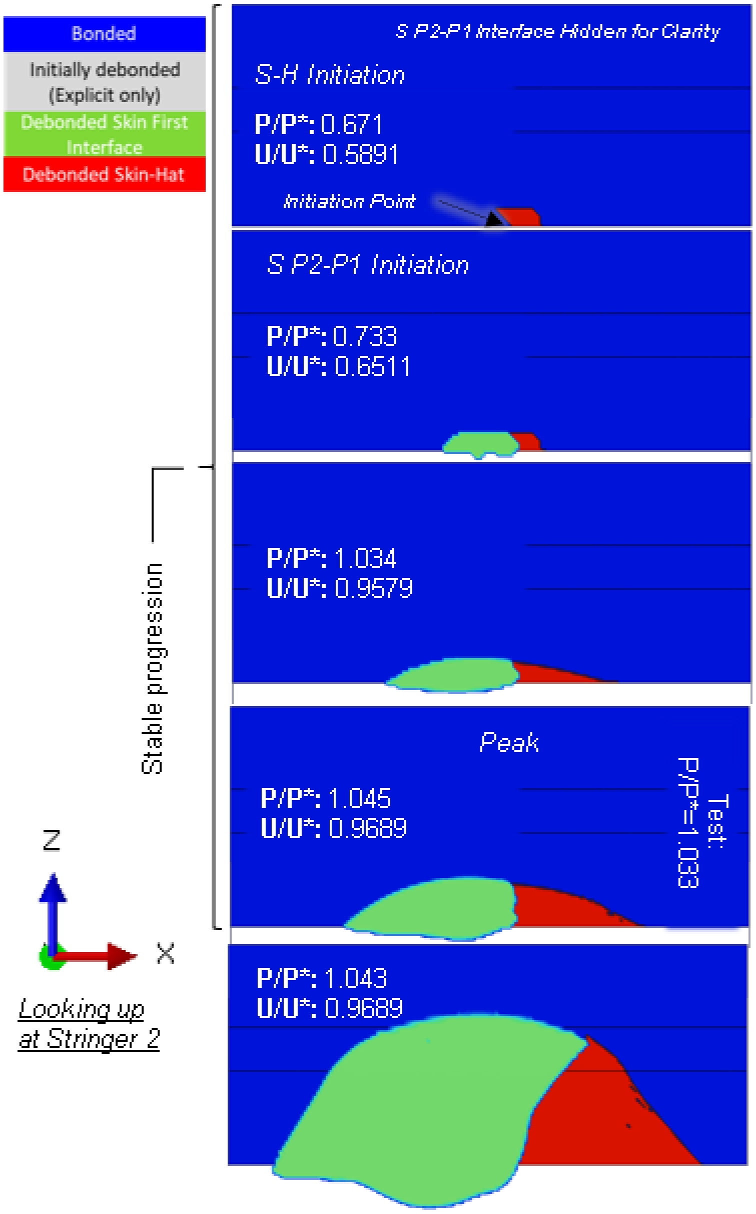

Figure 15. Debonding Plots of Impact Panel (Hat Stringer 2 shown from Bottom); Model IR1

Subsequently, the IR2 and IR3 refinement level models were also run. The resulting skin-hat initiation scaled loads and peak scaled loads are plotted versus the in-plane mesh density for these two methods in Figure 16. The peak load plateaus at a scaled value of roughly 1.07 between the IR2 and IR3 refinement levels. The initiation load cannot be correlated to the test since it was not included in the test report. Though the change certainly is slowing between the IR2 and IR3 models, it is not unexpected as it is known to be more sensitive to element edge length.

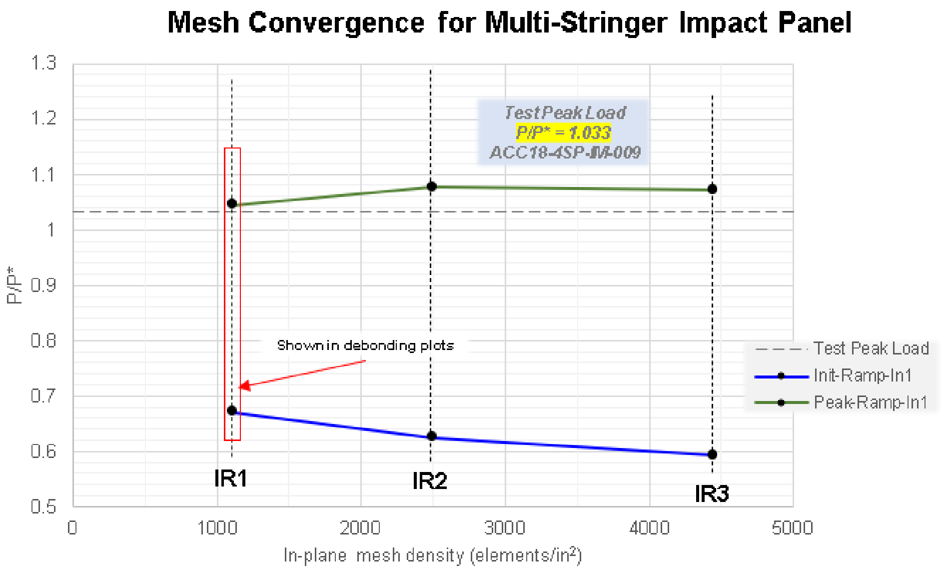

Figure 16. Mesh Convergence for Impacted Multi-Hat Stiffened Panel

Table 7 presents the results for the Impact specimen, including the processing time and number of CPUs used to run the simulation. The IR1 model produced the closest alignment to the test in terms of peak load (+1.2% error), but the "converged" load rises slightly to an average of +4.0% error when mesh density is increased to IR2 and IR3 levels. However, since the change is relatively small between the IR1 and IR2 models, yet the processing time increases significantly, the IR1 model is deemed viable for this analysis.

Table 7. Impact FEM Results Summary

Impact		S-H Init.	S P2-P1 Init.	Peak		Time to Peak	CPUs
Method	Model	P/P*	P/P*	P/P*	% Diff	hrs	
Ramp	IR1	0.671	0.733	1.045	1.2	11.4	24
	IR2	0.624	0.702	1.077	4.3	39.7	24
	IR3	0.593	0.679	1.071	3.7	31.3	36

The Teflon specimen in the test failed at an average peak scaled load of 1.000. The incremental UT debonding states for specimen ACC18-4SP-INS-011, as shown in Figure 5(b), demonstrate a stable progression of delamination in the Skin-Hat interface first and then the Skin first ply (Ply 2-Ply 1) interface. The Skin-Hat interface initiation scaled load was 0.912 for the TR1 model. After a short period of stable growth, the damage migrated the Skin Ply 2-Ply 1 interface, as observed in the testing. Then, the load reached a peak at a scaled load of 1.004, upon which the growth went unstable, and the delamination propagated rapidly without additional load increase.

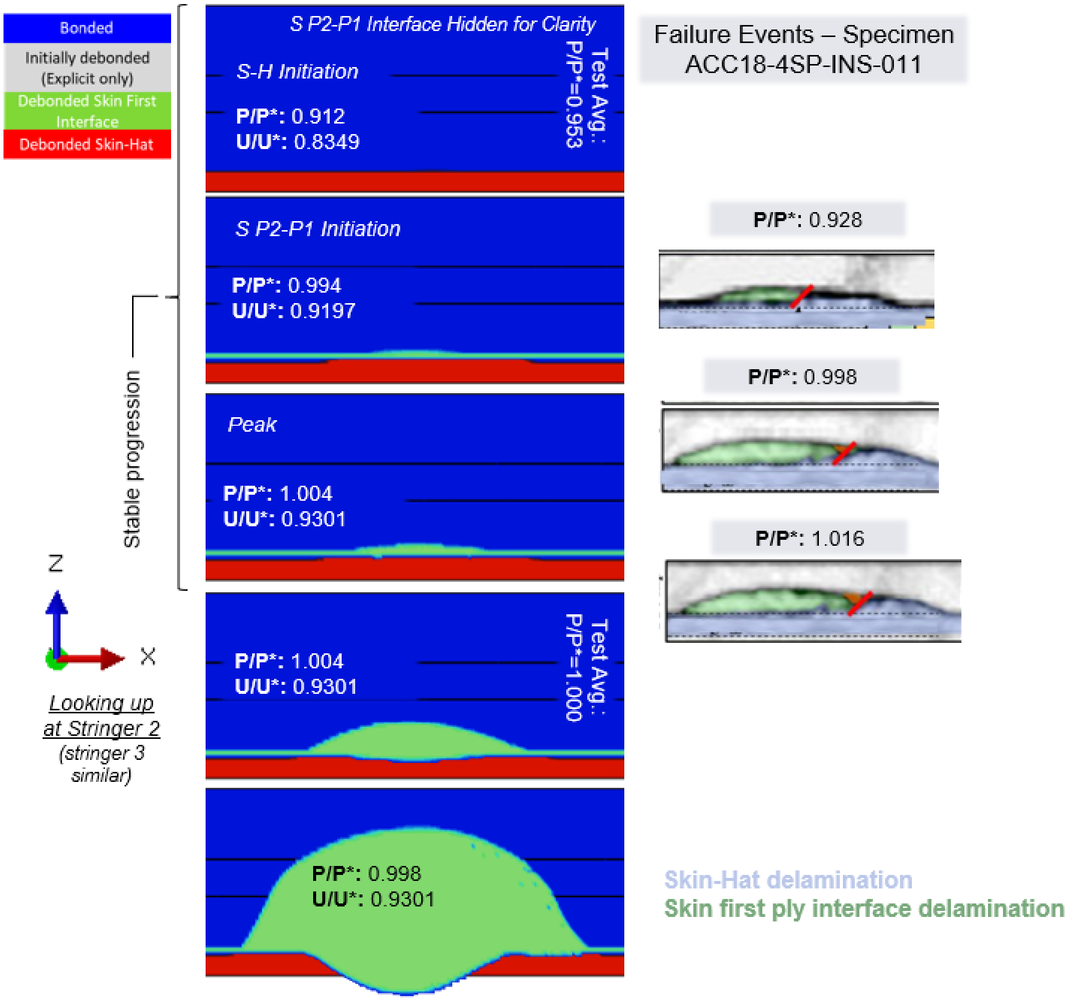

Figure 17. Debonding Plots of Teflon Panel (Hat Stringer 2 shown from Bottom); Model TR1. (Test data from Action et al. [18])

Subsequently, the TR0, TR2, and TR3 refinement level models were run using all three solution methods. The TR3 model ran for 977 hours on 48 CPUs but did not produce a peak load value. However, the simulation appeared to be converging to a peak in agreement with the mesh convergence behavior of the less refined models. The resulting skin-hat initiation scaled loads and peak scaled loads are plotted versus the in-plane mesh density for these methods in Figure 18. The behavior between the TR0, TR1, and TR2 models using Ramp indicates a mesh convergence around P/P*=0.98-1.00.

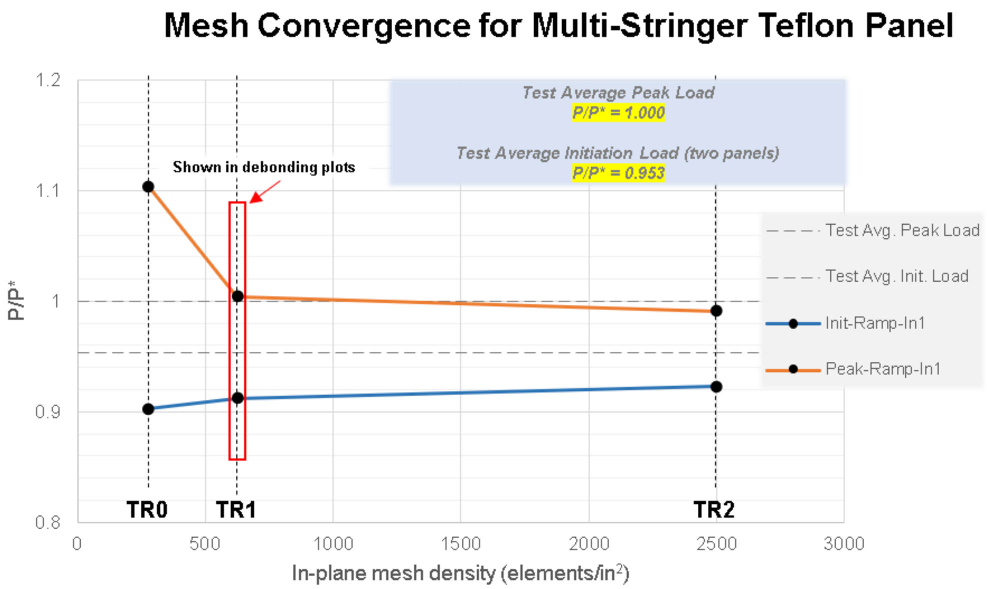

Figure 18. Mesh Convergence for Multi-Hat Stiffened Panel with Teflon Inserts

Table 8 presents all runs for the Teflon specimen, including the processing time and number of CPUs used to run the simulation. See the discussion on Ramp versus Step regarding the Impact runs. A previous effort (AIAA-Action/Leone 2020) sought to simulate the Teflon specimen behavior using CompDam. The resulting scaled peak load from the analysis was 1.053. Although it does not capture interlaminar damage behavior, the current effort used VCCT, a less computationally expensive method, producing good correlation with the test data. Therefore, the current method is presented as a viable alternative.

A small sacrifice in processing time but a large increase in accuracy and convergence behavior is observed from the TR0 to TR1 models. However, the TR2 model experiences an extremely large jump in processing time but minimal change in final peak load. Therefore, the TR1 model is viewed as the optimal model for this simulation.

Table 8. Teflon FEM Results Summary

Teflon		S-H Init.		S P2-P1 Init.	Peak		Time to Peak	CPUs
Method	Model	P/P*	% Diff	P/P*	P/P*	% Diff	hrs	
Ramp	TR0	0.90	-5.2	1.10	1.10	10.4	1.3	24
	TR1	0.91	-4.3	0.99	1.00	0.4	2.2	24
	TR2	0.92	-3.1	0.93	0.99	-0.9	146.1	48

The scaled load-displacement plot is given in Figure 19 for the Impact IR1 Ramp model (blue) and the Teflon TR1 Ramp model (red). As revealed in the plot, the Teflon specimen has a higher initiation load yet lower peak load than the Impact specimen, and in-turn, a much smaller load interval of stable delamination growth.

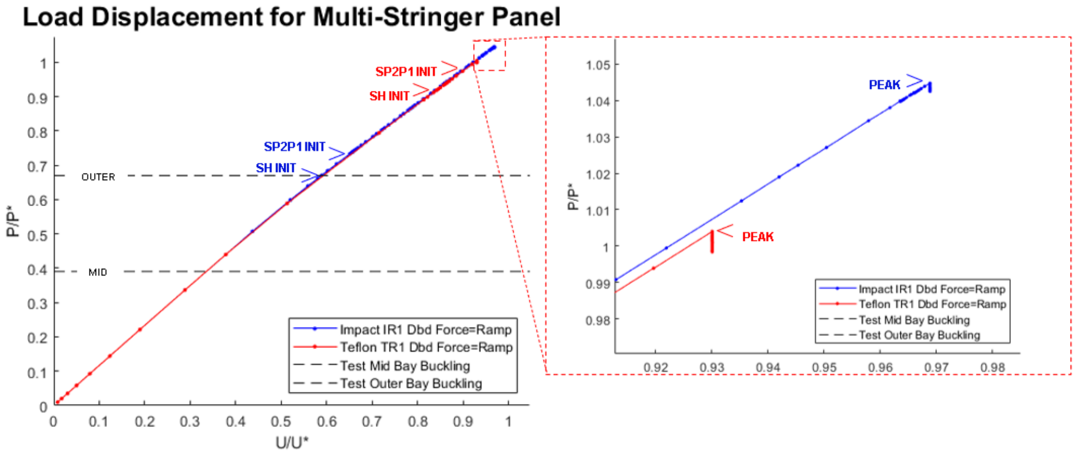

Figure 19. Load Displacement for Multi-Hat Stiffened Panel

CONCLUSIONS

Static testing of the multi-hat stiffened panel was previously conducted under the NASA ACP, where the configurations included Teflon inserts and compression after impact (CAI). This effort sought to use VCCT in Abaqus to show a reasonable comparison to the test behavior with a reasonably lightweight tool. The analysis utilized multiple VCCT interface definitions in Abaqus to capture damage initiation (beyond embedded damage) and progression in a post-buckled state. A study of the model strains versus strain gauge data from the testing showed good agreement (<10% error) in stiffness for key panel locations. In addition, the buckling loads showed agreement within 15%. Multiple model refinement levels, the Step debonding method in Abaqus/Standard, Ramp in Abaqus/Standard, and dynamic analysis using Abaqus/Standard Explicit were evaluated. The Ramp model was ultimately chosen for reasons described in the Results section. The peak load differences were within 5% and 1% for Teflon for impact. Numerous assumptions were made as inputs to the model, including the location and size of the initial damage. Overall, the authors recommend VCCT as a viable alternative to other costly PDA methods.

ACKNOWLEDGMENTS

The authors want to thank the Office of the Naval Research for their support under Award No. N00014-21-C-1007. Also, the authors are grateful to the NASA ACP Progressive Damage Analysis Cooperative Research Team for granting permission to use the experimental data completed under Award No. NNL09AA00A.

REFERENCES

1. Degenhardt R, Castro SGP, Arbelo MA, Zimmerman R, Khakimova R, Kling A., "Future structural stability design for composite space and airframe structures," Thin-Wall Structures, 2014, Vol 81(7).
2. Hao P, Wang B, Tian K, Li G, Du K, Luan Y., "Integrated optimization of hybrid stiffness stiffened shells based on sub-panel elements," Thin-Wall Structures, 2016, Vol 103.
3. Gliszczynski A, Kubiak T., "Progressive failure analysis of thin-walled composite columns subjected to uniaxial compression," Composite Structures, 2017, Vol 169.
4. Pietropaoli E, Riccio A, "A global/local finite element approach for predicting interlaminar and intralaminar damage evolution in composite stiffened panels under compressive load," Appl Compos Mater, 2011, Vol 18(2).
5. Gong Y, Zhang B, Hallett SR., "Delamination migration in multidirectional composite laminates under mode I quasi-static and fatigue loading," Compos Struct, 2018; Vol 189.
6. Gong Y, Zhao L, Zhang J, Wang Y, Hu N., "Delamination propagation criterion including the effect of fiber bridging for mixed-mode I/II delamination in CFRP multidirectional laminates," Compos Sci Technol, 2017, Vol 151.
7. Bisagni C, Vescovini R, Davila CG. "Development of a single-stringer compression specimen for the assessment of damage tolerance of postbuckled structures." J Aircraft, 2011, Vol 48(2).
8. Anyfantis KN, Tsouvalis NG. "Post buckling progressive failure analysis of composite laminated stiffened panels." Appl Compos Mater, 2012, Vol 19(3-4).
9. De Carvalho NV, Mabson GE, Krueger R, Deobald LR. "A new approach to model delamination growth in fatigue using the Virtual Crack Closure Technique without re-meshing." Eng Fract Mech, 2019, Vol 222.
10. Mabson GE, Deobald LR, Dopker B, Hoyt DM, Baylor JS, Graesser DL. "Fracture interface elements for static and fatigue analysis." Proceedings of 16th international conference on composite materials (ICCM16), Kyoto, 2007.
11. Di Memmo I, Bisagni C. “Fatigue simulation for damage propagation in composite structures.” Proceedings of 32nd technical conference of the American Society for Composites, West Lafayette, 2017, No. 135472.
12. Raimondo A, Doesburg SA, Bisagni C. "Numerical study of quasi-static and fatigue delamination growth in a post-buckled composite stiffened panel." Compos B Eng, 2019.
13. Camanho PP, Davila CG, de Moura M. "Numerical simulation of mixed-mode progressive delamination in composite materials." J Compos Mater, 2003, Vol 37.
14. Goyal VK, Pennington A, Action J, 2022, "Progressive Damage Failure Analysis of Post-Buckled Composite Single-Stringer Panel with Teflon Inserts," American

Society for Composites 36th Technical Conference, College Station, TX, September 19–21, 2021.

15. Goyal VK, Pennington A, Action J, 2022, "Damage Prediction of Post-Buckled Composite Single Hat-Stringer Panel Subject to Compression After Impact," AIAA Science and Technology Forum and Exposition 2022, San Diego, CA, AIAA 2022-2394.
16. Leone, FA, Song K, Rose CA, Jackson WC, "Progressive Damage Analysis of Post-Buckled Stiffened Panels under Static Compressive Loading," AIAA SciTech Forum, 6-10 January 2020, Orlando, FL.
17. Leone, FA, Song K, Johnston W, Rose CA, Jackson WC, Kosztowny CJ, Davila CG, "Test/Analysis Correlation of Damage States in Post-buckled Stiffened Validation Building Block Specimens," Proceedings of 34th technical conference of the American Society for Composites, 2019, No. 28086.
18. Action J, Palliyaguru U, Jackson W, Zalameda J, 2020, "Testing of a Multi-Stringer Post-Buckled Panel with Incremental Damage Detection," AIAA SciTech 2020 Technical Conference, Orlando, FL, 2020. AIAA 2020-1480.